Monthly Notices
of the
ROYAL ASTRONOMICAL SOCIETY

Mon. Not. R. Astron. Soc. **415,** 313–322 (2011) doi:10.1111/j.1365-2966.2011.18699.x

From proper motions to star cluster dynamics: measuring the velocity dispersion in deconvolved distribution functions

C. Bonatto★ and E. Bica

Departamento de Astronomia, Universidade Federal do Rio Grande do Sul, Av. Bento Gonçalves 9500 Porto Alegre 91501-970, RS, Brazil

Accepted 2011 March 11. Received 2011 March 11; in original form 2011 January 25

ABSTRACT

We investigate the effect that the usually large errors associated with ground-based proper motion (PM) components have on the determination of a star cluster's velocity dispersion (σ_v). Rather than histograms, we work with PM distribution functions (PMDFs), taking the 1σ uncertainties formally into account. In this context, a cluster's intrinsic PMDF is broadened by the error distribution function (eDF) that, given the average error amplitude, has a width usually comparable to the cluster PMDF. Thus, we apply a Richardson–Lucy (RL) deconvolution to the PMDFs of a set of relatively nearby and populous open clusters (OCs), using the eDFs as point spread functions. The OCs are NGC 1039 (M 34), NGC 2477, NGC 2516, NGC 2682 (M 67) and NGC 7762. The deconvolved PMDFs are approximately Gaussian in shape, with dispersions lower than the observed ones by a factor of 4–10. NGC 1039 and 2516, the nearest OCs of the sample, have deconvolved σ_v compatible with those of bound OCs of mass $\sim 10^3\,M_\odot$. NGC 2477 and 2682 have deconvolved PMDFs with a secondary bump, shifted towards higher average velocities, which may be an artefact of the RL deconvolution when applied to asymmetric profiles. Alternatively, it may originate from cluster merger, large-scale mass segregation or, least probably, binaries.

Key words: open clusters and associations: general.

1 INTRODUCTION

Star clusters continually undergo mass segregation and evaporation, tidal interactions with Galactic substructures, shocks with giant molecular clouds, as well as mass-loss due to stellar evolution. By decreasing the total cluster mass – and the collective gravitational potential – these processes affect the internal dynamics and accelerate the cluster dynamical evolution. Thus, the escape velocity ($v_{\rm esc}$) and, to a lesser degree, the space velocity dispersion (σ_v) are expected to continually change with time. As a consequence, the majority of the open clusters (OCs) dissolve in the Galactic stellar field long before reaching an age of $\sim$1 Gyr (e.g. Lamers et al. 2005; Goodwin & Bastian 2006). In this context, the dynamical evolution of a star cluster depends critically on the balance between σ_v and $v_{\rm esc}$.

For a cluster that is approximately in virial equilibrium, the space velocity dispersion can be computed as $\sigma_v\,({\rm km\,s^{-1}}) = \sqrt{\frac{GM_{\rm D}}{\eta R_{\rm eff}}} \approx 0.7(\frac{M_{\rm D}}{10^3\,{\rm M}_\odot})^{1/2}(\frac{R_{\rm eff}}{1\,{\rm pc}})^{-1/2}$ (Spitzer 1987), where G is the gravitational constant, $M_{\rm D}$ is the dynamical mass (assumed to be stored only in single stars), $\eta \approx 9.75$ is a constant and $R_{\rm eff}$ is the effective or projected half-light radius. As a scaling factor, bound clusters with $M_{\rm D} \sim 10^3\,{\rm M}_\odot$ and $R_{\rm eff} \sim 1$ pc are expected to have $\sigma_v \sim 1\,{\rm km\,s^{-1}}$. Since the majority of the Galactic OCs have masses lower than $10^3\,{\rm M}_\odot$ (e.g. Piskunov et al. 2007), velocity dispersions lower than or of the order of $\sigma_v \sim 1\,{\rm km\,s^{-1}}$ should be a rule.

Obviously, the above expectation does not apply to clusters that are on their way to dissolution, either at the earliest evolutionary stages (less than a few 10^7 yr) or much later, at the remnant phase (several 10^8 yr, e.g. Pavani & Bica 2007). Such a supervirial state in very young clusters is related to the impulsive expulsion of the residual parental molecular cloud gas, driven primarily by the strong winds of massive stars and supernovae (Goodwin & Bastian 2006), thus leading to the high dissolution rate of young clusters (e.g. Lada & Lada 2003). Examples of dissolving young OCs with velocity dispersions that by far exceed the expected dynamical value (de Grijs et al. 2008) are NGC 2244, with an age of $\sim$5 Myr and $\sigma_v \sim 35\,{\rm km\,s^{-1}}$ (Chen, de Grijs & Zhao 2007; Bonatto & Bica 2009b), and Cr 197 and vdB 92, both with an age of $\sim$5 Myr and $\sigma_v \sim 20\,{\rm km\,s^{-1}}$ (Bonatto & Bica 2010a).

A first-order estimate of a star cluster's σ_v can be obtained by measuring the proper-motion (PM) distribution of the member stars. Having obtained the PM components in right ascension [$\mu_\alpha \cos(\delta)$] and Declination (μ_δ) of each member, the $\sigma_\alpha \equiv \sigma_{\mu_\alpha \cos(\delta)}$ and $\sigma_\delta \equiv \sigma_{\mu_\delta}$ dispersions can be estimated from the shape of the respective distributions. Alternatively, if the systemic PM components are known, one can compute directly the tangential or on-sky

★E-mail: charles@if.ufrgs.br

PM $\mu_{\rm os} = \sqrt{\mu_\alpha \cos(\delta)^2 + \mu_\delta^2}$ and dispersion $\sigma_{\rm os} = \sqrt{\sigma_\alpha^2 + \sigma_\delta^2}$. Then, assuming isotropy, we can take $\sigma_v^2 = \frac{3}{2}(\sigma_\alpha^2 + \sigma_\delta^2) = \frac{3}{2}\sigma_{\rm os}^2$. At this point, it should be mentioned that, contrary to radial velocity measurements, PMs are essentially unaffected by binarity (Kouwenhoven & de Grijs 2008). This occurs because radial velocities are instantaneous measurements, while PMs involve a (usually large) time-span. In this sense, Kouwenhoven & de Grijs (2008) show that for clusters of mass $\sim$1000 $M_\odot$, binaries produce an observed radial velocity dispersion several times higher than the dynamical one, thus leading to an artificially overestimated cluster mass.

Comprehensive data bases such as The Third US Naval Observatory CCD Astrograph Catalog (UCAC3, Zacharias et al. 2010) and The Naval Observatory Merged Astrometric Dataset (NOMAD, Zacharias et al. 2004) provide PM components for huge amounts of stars, either isolated or in clusters. However, a drawback of such all-sky, ground-based PM data bases is the fact that the 1σ uncertainties in $\mu_\alpha \cos(\delta)$ and μ_δ are usually large. The effect that such errors have on the determination of σ_v, which usually involves building PM histograms with bin sizes smaller than the average 1σ errors, is a constantly neglected point. Instead of histograms, our approach in this paper is to work with PM distribution functions (PMDFs), in which the errors are formally taken into account.

This paper is organized as follows. In Section 2, we build PMDFs and compare them with the classical histograms. In Section 3, we select some relatively nearby and populous OCs as test cases. In Section 4, we discuss the deconvolution method that we apply on the PMDFs. In Section 5, we present the results obtained so far and discuss some observational limitations. Concluding remarks are given in Section 6.

2 PROPER MOTION ANALYSIS: HISTOGRAMS OR DISTRIBUTION FUNCTIONS?

When dealing with PMs, the first step is to isolate the (most probable) cluster members, subtract the systemic components of $\mu_\alpha \cos(\delta)$ and μ_δ from each star, and then compute the tangential or on-sky PM $\mu_{\rm os}$. The systemic components can be directly computed from the data or obtained in OC data bases (e.g. WEBDA[1] or DAML02[2]).

Usually, the next step involves building PM histograms with a given bin width to estimate the dispersion either of the right ascension and declination components or the projected on-sky. However, except for a few particular cases with high-quality astrometry,[3] ground-based PMs usually have significant errors, in general larger than the adopted histogram bins. Thus, by ignoring the error amplitude, histograms should be taken only as first-order representatives of a cluster's intrinsic PM distribution. Wider bins would obviously minimize this effect, but would also degrade the PM resolution. The net result would be artificially high values of the dispersion. This is illustrated in Fig. 1 for the $\mu_\alpha \cos(\delta)$ component of the OCs NGC 2682 and 2477 (Section 3), where we show the classical histogram built with bins of size $\Delta\mu_\alpha \cos(\delta) = 1$ mas yr^{-1}. Also shown are the average, minimum and maximum values of the 1σ errors. Clearly, in both cases, the average 1σ error corresponds to approximately the core (approximately four bins) of the histogram. It should be noted as well the introduction of a sort of high-frequency noise, which originates from the Poisson fluctuation associated with the bin size.

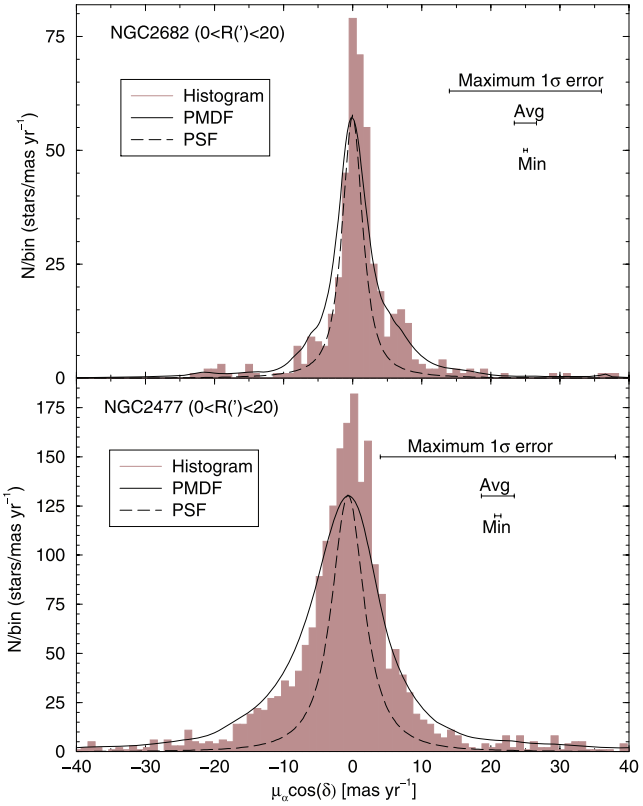

Figure 1. Histogram and PMDF (heavy solid line) of NGC 2682 (top panel) and NGC 2477 (bottom panel) for the stars located within $R < 20$ arcmin. The amplitudes of the maximum, average and minimum 1σ errors are illustrated (horizontal lines). Also shown is the error distribution function (dashed line).

Thus, instead of histograms, the correct way of dealing with the above issue is by explicitly incorporating the PM component errors in PMDFs, which are defined as the fractional number of stars *per* interval of the PM, PMDF $\equiv \phi(\mu) = {\rm d}N/{\rm d}\mu$, where μ is any component among $\mu_\alpha \cos(\delta)$, μ_δ and $\mu_{\rm os}$. The errors are incorporated in the PMDFs by assuming that they are normally (i.e. Gaussian) distributed. Accordingly, if measurements of a given parameter χ are normally distributed around the average $\bar{\chi}$ with a standard deviation ϵ, the probability of finding it at a specific value χ is given by $P(\chi) = \frac{1}{\sqrt{2\pi}\epsilon} {\rm e}^{-\frac{1}{2}(\frac{\chi-\bar{\chi}}{\epsilon})^2}$.

We start by defining a set of PM bins spanning the whole range of values observed in $\mu_\alpha \cos(\delta)$, μ_δ and $\mu_{\rm os}$. The bins have smaller widths around the PMDF peak than for higher or lower velocities (for preserving the profile resolution – Appendix A). Then, for a star with PM components and 1σ uncertainties $\mu_\alpha \cos(\delta) \pm \epsilon_{\mu_\alpha \cos(\delta)}$, $\mu_\delta \pm \epsilon_{\mu_\delta}$, $\mu_{\rm os} \pm \epsilon_{\mu_{\rm os}}$, we compute the probability of the PM of that star to be in a given bin, which is simply the difference of the error functions computed at the bin borders. By doing this for all stars, we end up with the number density of stars in each PM bin, the integral of which over the whole range of PM values is simply the number of stars. The $\mu_\alpha \cos(\delta)$ PMDFs of NGC 2682 and 2477 are shown in Fig. 1. By construction, the PMDFs are much smoother than the histograms (the high-frequency noise has been naturally removed) and, because of the broadening effect due to the error spreading procedure, they are also somewhat wider and have a

[1] www.univie.ac.at/webda

[2] Catalog of Optically Visible Open Clusters and Candidates, www.astro.iag.usp.br/ wilton

[3] For instance, the globular cluster NGC 6397 with *Hubble Space Telescope* WFPC2 data from two epochs (Richer et al. 2008).

Table 1. Fundamental parameters and cluster systemic PM components derived in this work.

	Literature						This work				
Cluster	α(2000) ($^{\rm h}\,^{\rm m}\,^{\rm s}$)	δ(2000) ($^\circ\,'\,''$)	ℓ ($^\circ$)	b ($^\circ$)	Age (Myr)	A_V (mag)	$d_\odot$ (kpc)	$R_{\rm RDP}$ (pc)	$R = 5$ arcmin (pc)	$[\mu_\alpha \cos(\delta)]_{\rm syst}$ (mas yr^{-1})	$(\mu_\delta)_{\rm syst}$ (mas yr^{-1})
(1)	(2)	(3)	(4)	(5)	(6)	(7)	(8)	(9)	(10)	(11)	(12)
NGC 1039	02:42:45	+42:45:42	143.66	−15.61	300 ± 50	0.2 ± 0.2	0.49 ± 0.03	4.3 ± 0.7	0.7	−0.55 ± 0.01	−5.81 ± 0.01
NGC 2477	07:52:10	−38:31:48	253.56	−5.84	900 ± 100	0.8 ± 0.2	1.31 ± 0.07	13.3 ± 1.9	1.9	−0.83 ± 0.07	+1.89 ± 0.06
NGC 2516	07:58:04	−60:45:12	273.82	−15.86	200 ± 50	0.3 ± 0.2	0.38 ± 0.04	3.3 ± 0.3	0.6	−5.60 ± 0.07	+10.74 ± 0.03
NGC 2682	08:51:18	+11:48:00	215.70	+31.90	4000 ± 300	0.0 ± 0.1	0.79 ± 0.05	6.9 ± 0.7	1.2	−8.61 ± 0.02	−4.92 ± 0.05
NGC 7762	23:50:01	+68:08:18	117.22	+5.85	2000 ± 500	1.4 ± 0.4	0.96 ± 0.14	7.0 ± 1.4	1.4	−4.67 ± 0.01	−2.53 ± 0.03

Notes. Columns (4) and (5): Galactic coordinates; Column (8): distance from the Sun; Column (9): cluster truncation radius (in pc); Column (10): $R = 5$ arcmin in absolute units; Columns (11) and (12): deconvolved systemic PM components, computed with the stars within $R < 20$ arcmin.

lower amplitude. Both the histograms and PMDFs are definitely non-Gaussian, especially because of the broad wings.

Now, the same procedure is applied to the uncertainties, thus resulting in the intrinsic error distribution function (eDF). As anticipated by the amplitude of the average 1σ error, the eDF has a width comparable to that of the PMDF for both NGC 2682 and 2477. In this context, the eDF plays a role of a PM point spread function (PSF), which tends to broaden the intrinsic cluster PMDF on a degree that depends essentially on the PMDF and eDF widths. Thus, our approach here is to deconvolve the observed PMDF of selected OCs (Section 3) using the intrinsic eDF as the PSF (Section 4).

3 TEST CASES

As test cases, we searched for OCs that are located relatively nearby (for allowing the detection of low-PM components – Section 5), away from central directions and the disc (to minimize the field-star contamination), and with a wide range of ages. Additionally, the candidates should have a significant number of stars with available PM components in UCAC3[4] (for more representative PMDFs). The OCs meeting our criteria are NGC 1039 (M 34), NGC 2477, NGC 2516, NGC 2682 (M 67) and NGC 7762; their fundamental parameters are listed in Table 1. In short, the selected OCs have ages within 0.2–4 Gyr and distances from the Sun within ∼0.4–1.3 kpc.

2MASS[5] (Skrutskie et al. 2006) colour–magnitude diagrams (CMDs) extracted from the central region ($R < 5$ arcmin) are shown in Fig. 2. The 5-arcmin boundary was selected for practical reasons. Our analysis depends on the number of member stars in two different cluster regions (Section 4) and the stellar density profiles (Fig. 3) show that $R = 5$ arcmin represents a compromise between adequate statistics and a change from radial density profiles (RDPs) following a pure power law ($R \gtrsim 5$ arcmin) to a power law flattened by a core ($R \lesssim 5$ arcmin). For NGC 2682 (M 67), we also use the ground-based CCD astrometry of Yadav et al. (2008) as an independent data set for cross-checking our results. The PM components provided by Yadav et al. (2008) are already corrected for the cluster's systemic velocity. The 2MASS photometry was extracted from VizieR[6] in a wide circular field of radius $R_{\rm ext} = 90$ arcmin, which

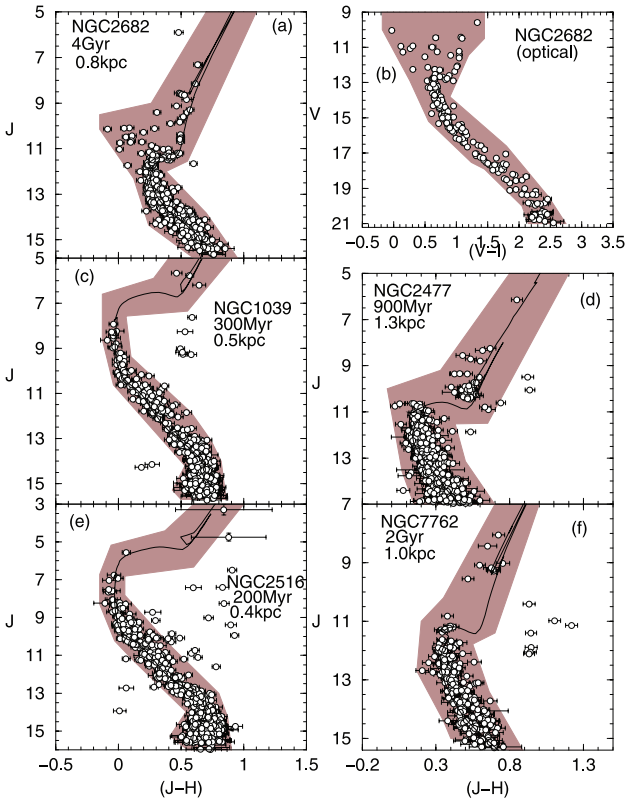

Figure 2. Extracted within $R < 5$ arcmin, the CMDs have been built with 2MASS photometry, except for panel (b) that was built with the VI CCD photometry of Yadav et al. (2008). Only stars that occur within the colour–magnitude filter (shaded polygon) are considered in the analyses.

is adequate for determining the cluster extension and background level (see below). We also build a colour–magnitude filter for each cluster, which is used to isolate probable member stars (see e.g. Bonatto & Bica 2010b for a discussion on the use of such filters). Only stars with colour and magnitude compatible with the filter are used in the subsequent analyses. The sge, distance from the Sun and reddening are derived by fitting solar-metallicity Padova isochrones (Girardi et al. 2002; Bonatto, Bica & Girardi 2004) to the CMDs. The derived fundamental parameters (Table 1) are similar to those in the WEBDA.

After isolating the probable member stars with the colour–magnitude filters, we use them to build the stellar RDP, which is the projected stellar number density profile around the cluster centre (Fig. 3). Note that the cluster centres have been computed

[4] Main features of UCAC3 are complete sky coverage, merging of several PM catalogues, new data reduction with reduced errors, significantly improved photometry from CCD data, etc. See http://cdsarc.u-strasbg.fr/viz-bin/Cat?I/315 for further details.

[5] The Two-Micron All-Sky Survey, All-Sky data release – http://www.ipac.caltech.edu/2mass/releases/allsky/

[6] http://vizier.u-strasbg.fr/viz-bin/VizieR?-source = II/246

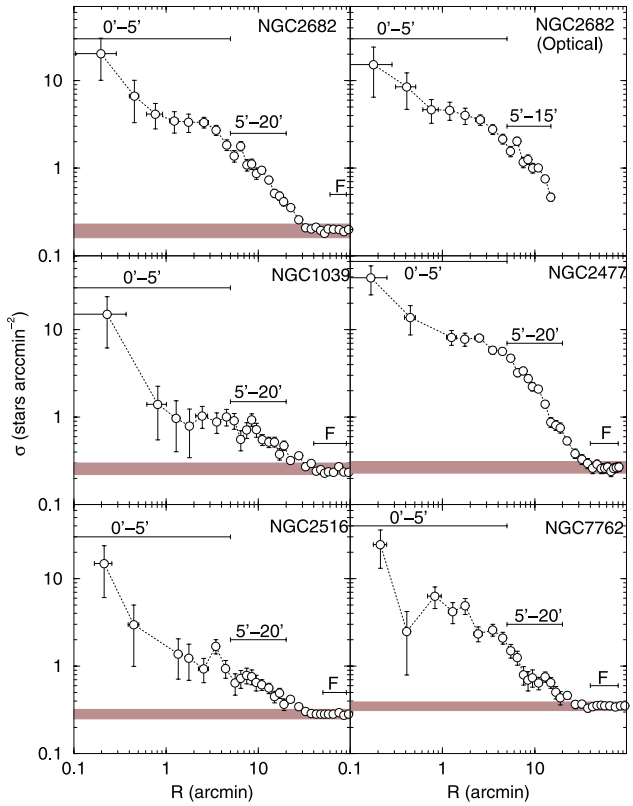

Figure 3. Stellar RDPs of the selected OCs. The central [$0 < R$(arcmin) < 5], outer [$5 < R$(arcmin) < 20 or $5 < R$(arcmin) < 15 (top right-hand panel)] and field (F) regions are indicated. The field contamination level towards the central parts is illustrated by the shaded polygon.

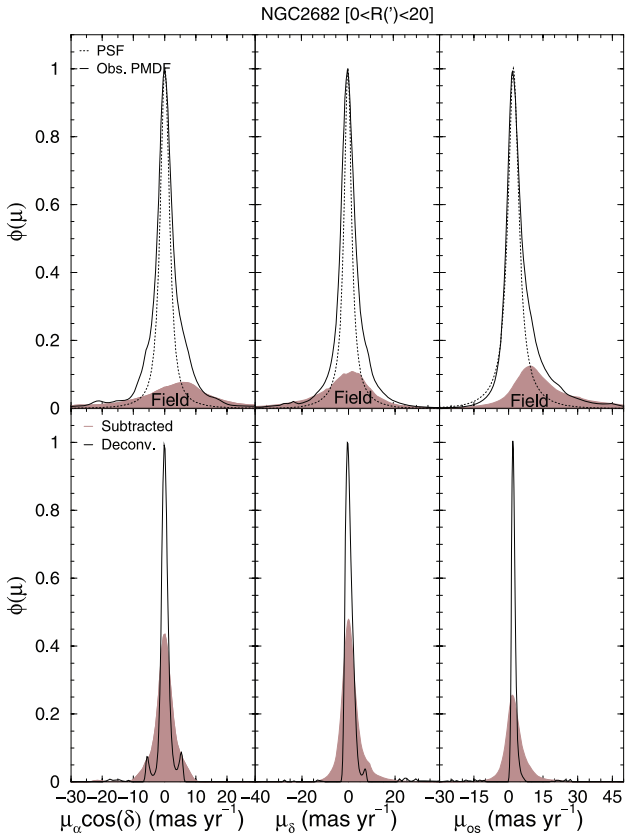

Figure 4. RL deconvolution applied to the $\mu_\alpha \cos(\delta)$ (left-hand panel), μ_δ (middle panel) and $\mu_{\rm os}$ (right-hand panel) PM components for the stars located in the region $R < 20$ arcmin of NGC 2682. Top panels: observed cluster (solid line) and field (shaded area) PMDFs, and the PSF (dotted line). Bottom panels: field-subtracted (shaded area) and deconvolved (solid line) PMDFs.

by an algorithm that searches for the highest stellar density in the innermost bin and, at the same time, the smoothest RDP (Bonatto & Bica 2010a). Working with colour–magnitude filtered photometry minimizes field contamination and enhances the RDP contrast with the fore/background. The position (and error) of each RDP point along the R axes in Fig. 3 corresponds to the average (and 1σ uncertainty) distance to the cluster centre of the stars within each bin. We also estimate the cluster truncation radius ($R_{\rm RDP}$), which is simply the distance from the cluster centre where the RDP and background are statistically indistinguishable (Fig. 3). On average, the boundary $R = 5$ arcmin represents $\approx$1/6 of $R_{\rm RDP}$ (Table 1). The near-infrared RDPs show that the selected OCs have an extension reaching $\approx$20–30 arcmin (the optical data of Yadav et al. 2008 are restricted to $\approx$15 arcmin). They also show that field stars with the same colour and magnitude as the probable members are still present in the central region, in varying amounts for the different OCs. The residual field contamination will be taken into account in the PM analysis (Section 4).

PM components were obtained in UCAC3 (that also provides the 2MASS photometry for each star) based on the same central coordinates and extraction radius as those used for building the CMDs and RDPs. Afterwards, we applied the respective colour–magnitude filters (Fig. 2) before computing the PM distributions (see below).

4 PMDF DECONVOLUTION

By construction, the observed PMDFs are broadened by a PSF that corresponds to the eDF (Section 2). Thus, to uncover the intrinsic PMDFs, we apply the iterative Richardson–Lucy (RL) deconvolution method proposed by Richardson (1972) and Lucy (1974). The RL deconvolution conserves the PMDF integral (in the present context the number of stars), but has a relatively slow convergence rate.

We illustrate the RL deconvolution with the $\mu_\alpha \cos(\delta)$, μ_δ and $\mu_{\rm os}$ components of the OC NGC 2682 (Fig. 4). As the first step, we define the PM-bin size distribution (Appendix A), and compute and subtract the systemic PM components (Table 1) from $\mu_\alpha \cos(\delta)$ and μ_δ. Actually, this is an iterative step, in which we first subtract the field contamination, deconvolve the resulting PMDF and obtain the systemic PM. We use the region $R < 20$ arcmin in the analysis as a compromise between the number of member stars and contrast with the field level (Fig. 3). Then we build the cluster and field PMDFs, together with the eDF, which has a width similar to that of the cluster PMDF. Next, the contaminant PMDF of the residual field stars, which is especially seen in $\mu_\alpha \cos(\delta)$ as a bump centred at $\approx$6 mas yr^{-1}, is subtracted from the observed PMDFs. Finally, the RL deconvolution is applied to the field-subtracted PMDF.

Besides the slow convergence rate, the RL deconvolution is also known for not having a universal convergence criterion. Thus, for determining the number of deconvolution iterations ($N_{\rm it}$), we simply sum the squared difference between successive iterations over all bins of the deconvolved PMDF, defined as

$$\chi^2_j = \sum_i \left[{\rm PMDF}(x_i)_j - {\rm PMDF}(x_i)_{j-1}\right]^2,$$

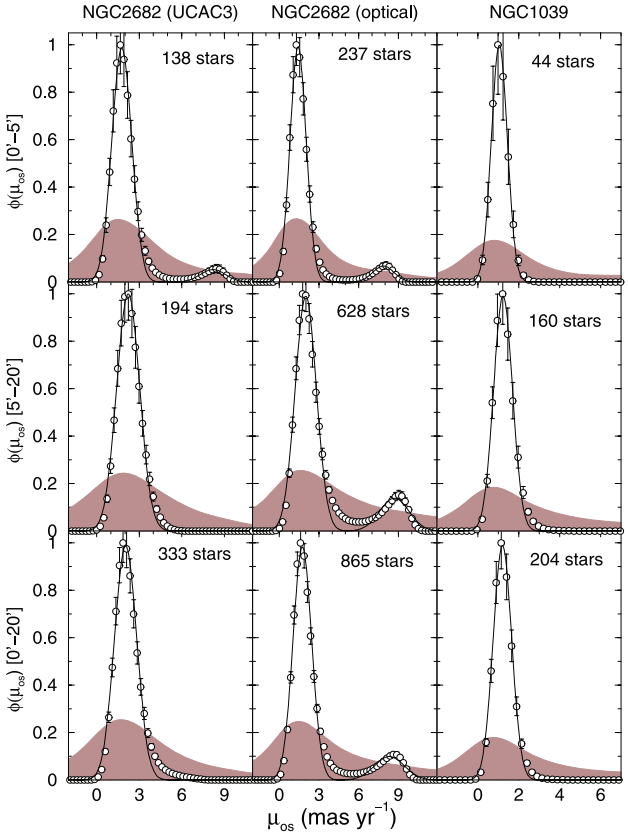

Figure 5. Field-subtracted (shaded area) and deconvolved (circles) on-sky PMDFs built for different cluster regions: central (top panel panels), outer (middle panels) and overall (bottom panels). The solid line shows the Gaussian fit to the deconvolved PMDF. The number of member stars in each region is indicated. The PMDFs with the optical data of Yadav et al. (2008) for NGC 2682 (central panels) are restricted to $R < 15$ arcmin.

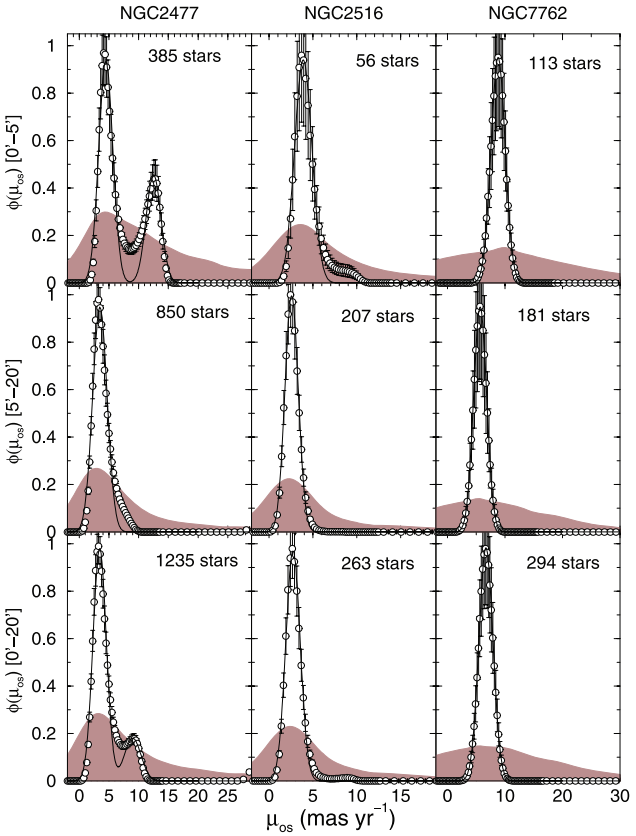

Figure 6. Same as Fig. 5 for the remaining clusters.

where j is the current iteration and x_i is the ith bin along the PM axis [either $\mu_\alpha \cos(\delta)$, μ_δ or $\mu_{\rm os}$], and compute the fractional variation of $\chi, f_\chi = 1 - \chi_j/\chi_{j-1}$. After a series of tests to check changes in deconvolution parameters with the number of iterations, we arbitrarily decided to stop when $N_{\rm it} = 200$ (or $f_\chi = 0.003$–0.005; Appendix A). Under this criterion, the deconvolved PMDFs end up with significantly lower dispersions than the observed ones (Figs 4–6 and Table 2), without significant added noise or artefacts (Appendix A). Besides, contrary to the observed PMDFs, the shape of the deconvolved ones is approximately Gaussian.

5 DISCUSSION

Similarly to NGC 2682 (Section 4), the RL deconvolution was applied to the field-subtracted PMDFs of the remaining OCs. Here we present the results of this procedure but, to avoid redundancy, we restrict the discussion to the on-sky PMDFs. However, besides the overall cluster, we also analyse separately the central and outer regions (according to the RDPs in Fig. 3), to search for spatial variations in the stellar kinematics that may be related to dynamical evolution. The deconvolved PMDFs are subsequently fitted with a Gaussian profile PMDF(μ) $\propto e^{-0.5[(\mu-\bar{\mu})/\sigma]^2}$, which provides the velocity dispersion (σ) and the average velocity ($\bar{\mu}$) of the stars in the region. The field-subtracted and deconvolved PMDFs are shown in Figs 5 and 6, and the relevant profile parameters are given in Table 2. The observed, field and error PMDFs for the full OC sample are shown in Appendix B.

It is clear that the deconvolved PMDFs (with dispersion $\sigma_{\rm dec}$) are significantly narrower than the field-subtracted ones ($\sigma_{\rm obs}$). Indeed, we find $\sigma_{\rm dec} \approx (0.1$–$0.25)\sigma_{\rm obs}$, but this ratio should be taken as an upper limit, since the observed PMDFs are not Gaussian and the fit is dominated by the profile core.

The central and outer parts of NGC 1039, 2516 and 7762, have PMDFs essentially characterized by a single Gaussian. In some cases (NGC 2682, 2477 and only marginally in 2516), however, the observed PMDF has a wing towards high-PM values, which appears to be a signature of the structure in the profile. This structure shows up in the deconvolved PMDFs as a second PM component, which is conspicuous especially in the central cluster region. The second component is characterized by a higher average velocity than the main one, but both have similar values of dispersion.

In the central parts of NGC 2477, the second component corresponds to about 40 per cent of the member stars in the region. This fraction drops to ∼17 per cent when the overall cluster is considered. For NGC 2682, this component contains only ∼7 per cent of the stars in the central region. This fraction is consistently the same for the UCAC3 and optical data. However, in the outer parts of NGC 2682, the second component is only seen in the optical data. Possible reasons for the difference are as follows: the optical PMDF corresponds to a smaller and somewhat more interior region (5–15 arcmin as compared to 5–20 arcmin), and contains approximately three times as much stars as that in UCAC3. The bump appears only when the observed PMDF is clearly non-asymmetric with respect to the average velocity, thus displaying a broad wing towards high velocities, for example, NGC 2477 and 2682. On the

Table 2. On-sky PM components.

		Observed		Deconvolved				
Region (arcmin) (1)	N (stars) (2)	$\bar{\mu}$ (mas yr^{-1}) (3)	σ (mas yr^{-1}) (4)	$\bar{\mu}$ (mas yr^{-1}) (5)	σ (mas yr^{-1}) (6)	$\bar{\mu}$ (km s^{-1}) (7)	σ (km s^{-1}) (8)	$\sigma_{obs}/\sigma_{dec}$ (9)
NGC 1039 – age $\sim$ 300 Myr, $d_\odot \sim 0.5$ kpc								
0–20	204	$\approx$1.2	$\gtrsim$2.4	1.20 ± 0.04	0.45 ± 0.04	2.8 ± 0.1	1.0 ± 0.1	$\gtrsim$5.1
5–20	160	$\approx$1.2	$\gtrsim$2.5	1.23 ± 0.04	0.46 ± 0.04	2.9 ± 0.1	1.1 ± 0.1	$\gtrsim$5.2
0–5	44	$\approx$1.0	$\gtrsim$1.9	1.05 ± 0.04	0.39 ± 0.04	2.4 ± 0.1	0.9 ± 0.1	$\gtrsim$4.9
NGC 2477 – age $\sim$ 900 Myr, $d_\odot \sim 1.3$ kpc								
0–20	1030	$\approx$3.3	$\gtrsim$5.3	3.44 ± 0.05	1.12 ± 0.05	21.4 ± 0.3	6.9 ± 0.3	$\gtrsim$4.6
0–20	205	–	–	9.00 ± 0.50	1.40 ± 0.40	55.9 ± 3.1	8.7 ± 2.5	–
5–20	850	$\approx$2.8	$\gtrsim$4.8	3.48 ± 0.04	1.22 ± 0.04	21.7 ± 0.3	7.6 ± 0.3	$\gtrsim$3.9
0–5	232	$\approx$4.5	$\gtrsim$7.5	4.47 ± 0.05	1.19 ± 0.05	27.8 ± 0.3	7.4 ± 0.3	$\gtrsim$6.0
0–5	153	–	–	12.5 ± 0.5	1.25 ± 0.25	77.6 ± 3.1	7.8 ± 1.6	–
NGC 2516 – age $\sim$ 200 Myr, $d_\odot \sim 0.4$ kpc								
0–20	263	$\approx$2.7	$\gtrsim$3.6	2.72 ± 0.02	0.82 ± 0.02	4.9 ± 0.1	1.5 ± 0.1	$\gtrsim$4.3
5–20	207	$\approx$2.5	$\gtrsim$3.4	2.56 ± 0.02	0.76 ± 0.02	4.6 ± 0.1	1.4 ± 0.1	$\gtrsim$4.5
0–5	56	$\approx$4.1	$\gtrsim$4.2	3.89 ± 0.02	0.99 ± 0.02	7.0 ± 0.1	1.8 ± 0.1	$\gtrsim$4.2
NGC 2682 (UCAC3) – age $\sim$ 4 Gyr, $d_\odot \sim 0.8$ kpc								
0–20	333	$\approx$2.1	$\gtrsim$3.2	2.04 ± 0.02	0.78 ± 0.03	7.6 ± 0.1	2.9 ± 0.1	$\gtrsim$4.1
5–20	194	$\approx$2.2	$\gtrsim$3.5	2.22 ± 0.03	0.81 ± 0.03	8.3 ± 0.1	3.0 ± 0.1	$\gtrsim$4.3
0–5	129	$\approx$1.9	$\gtrsim$2.8	1.77 ± 0.03	0.70 ± 0.03	6.6 ± 0.1	2.6 ± 0.1	$\gtrsim$4.0
0–5	9	–	–	8.20 ± 0.24	0.88 ± 0.24	30.7 ± 0.9	3.3 ± 0.9	–
NGC 2682 (optical)								
0–15	752	$\approx$1.4	$\gtrsim$3.4	1.75 ± 0.02	0.70 ± 0.02	6.6 ± 0.1	2.6 ± 0.1	$\gtrsim$4.9
0–15	113	–	–	8.32 ± 0.17	1.13 ± 0.17	31.1 ± 0.6	4.2 ± 0.6	–
5–15	535	$\approx$1.7	$\gtrsim$4.1	2.01 ± 0.03	0.80 ± 0.03	7.5 ± 0.1	3.0 ± 0.1	$\gtrsim$5.1
5–15	93	–	–	8.69 ± 0.15	1.10 ± 0.15	32.5 ± 0.6	4.1 ± 0.6	–
0–5	217	$\approx$1.3	$\gtrsim$2.4	1.43 ± 0.02	0.61 ± 0.02	5.4 ± 0.1	2.3 ± 0.1	$\gtrsim$4.0
0–5	20	–	–	7.86 ± 0.16	0.80 ± 0.16	29.4 ± 0.6	3.0 ± 0.6	–
NGC 7762 – age $\sim$ 2 Gyr, $d_\odot \sim 1.0$ kpc								
0–20	294	$\approx$6.4	$\gtrsim$11.8	6.70 ± 0.02	1.22 ± 0.02	30.1 ± 0.1	5.5 ± 0.1	$\gtrsim$9.7
5–20	181	$\approx$5.5	$\gtrsim$11.2	5.69 ± 0.02	1.13 ± 0.02	25.6 ± 0.1	5.1 ± 0.1	$\gtrsim$10
0–5	113	$\approx$8.5	$\gtrsim$12.7	8.81 ± 0.02	1.23 ± 0.02	39.6 ± 0.1	5.5 ± 0.1	$\gtrsim$10

Notes. Column (2): number of member stars in the region. $\bar{\mu}$ and σ were derived from the fit PMDF(μ) $\propto e^{-0.5[(\mu-\bar{\mu})/\sigma]^2}$. Conversion from mas yr^{-1} to km s^{-1} was based on the respective cluster distances (Table 1).

other hand, there is no bump emerging from the essentially Gaussian (observed) PMDFs of NGC 1039, 2516 and 7762 (Figs 5 and 6). In addition, it is interesting to note that the bump in the central region of NGC 2682 appears almost identically in PMDFs built with independent data sets.

Another issue is to what degree the incompleteness in crowded regions – and the more difficult measurement of PM components for faint stars – affects the PMDFs. Additionally, could the bump be related to incompleteness? We use NGC 2477, the most distant and populous OC of our sample (thus, the most prone to suffering from incompleteness), to examine this point (Appendix B). Since our analysis depends on the number of member stars (especially at the central region), we selected $J = 12.5$ as the boundary between bright and faint stars. At the distance of NGC 2477, this boundary corresponds to a stellar mass of $m \approx 1.6\,M_\odot$. The bright and faint deconvolved PMDFs built for the central region are similar (Fig. B3), consistently presenting the high-velocity bump at $\bar{\mu} \approx 12$ mas yr^{-1}. The only significant difference is that the faint (less-massive) star PMDF is shifted $\sim$1.3 mas yr^{-1} towards high values of $\bar{\mu}$ with respect to that of the bright stars. A similar shift occurs for the bright and faint star PMDFs in the outer region (without the bump). Although relatively small, the shift $\Delta\bar{\mu} \approx 1.3$ mas yr^{-1} ≈ 8 km s^{-1} between the bright and faint PMDFs might suggest slightly different kinematics for stars in different mass ranges. This experiment also suggests that incompleteness and PM measurements of faint stars – at least to the level available in UCAC3 – are not critical for the PMDFs.

Additionally, one might ask whether the bump may come from residual that is unaccounted for the field contamination. It is true that, given the statistical way we *decontaminate* the clusters (Section 3), some field-star contribution might persist in the subtracted PMDFs. However, both NGC 2477 and 2782 are located in the third Galactic quadrant and at high Galactic latitudes, which by itself minimizes contamination (as can also be seen in Figs B1 and B2). Thus, any residual contamination should be minimum, which would contradict the fraction of stars composing the bump, $\approx$40 per cent in the central region of NGC 2477 and $\approx$7 per cent in NGC 2682. The above arguments suggest that the bump is related to a cluster

kinematic property, but we cannot definitely rule out the possibility that it might be an artefact of the RL deconvolution and/or some residual contamination by stars with peculiar PM components.

There is no direct interpretation for the additional bump seen in the deconvolved PMDFs of NGC 2477 and 2682. Assuming that it is physical, one possibility is that the double peak may arise from a merger of two clusters (as suggested by the referee, Thijs Kouwenhoven). In this sense, de Oliveira, Bica & Dottori (2000) carried out *N*-body simulations of cluster encounters, studying long-term structural changes up to ∼1 Gyr. They found that the clusters may coalesce at such ages, but until then, the presence of the two clusters can still be traced by means of isophotal distortions and ellipticity variations, as observed in model and actual clusters (e.g. de Oliveira et al. 2000). In this scenario, internal differences in kinematics might persist too, producing different signatures in the deconvolved PMDFs.

Alternatively, the high-average-velocity component may be related to mass segregation, in which a fraction of the stars collectively migrate along the radial direction (over a time-scale of a relaxation time) within a star cluster. In the cases dealt with here, it occurs only in the two most populous OCs, NGC 2477 and 2682. Maybe it cannot be detected (by the present approach) in the other OCs because they are less populated (i.e. possibly the same reason why it is seen in the outer parts of NGC 2682 with the optical data, but not with UCAC3). Finally, working with histograms and a different PM data set, Bica & Bonatto (2005) raised the possibility that the high-velocity component in NGC 2682 might be related to the presence of binaries. However, given the findings of Kouwenhoven & de Grijs (2008), this possibility seems the least probable. In any case, a definitive solution for the bump nature would require detailed simulations of the internal cluster dynamics (including cluster merger, mass segregation and binarity), a task that is beyond the scope of this paper.

The velocity dispersions derived from the deconvolved PMDFs (Table 2) of NGC 1039 and 2516 (and, to a lesser degree, NGC 2682) are consistent with those of (approximately virialized) OCs of $\sim 10^3\,M_\odot$. On the other hand, those of NGC 2516 and 2477 appear to be excessively high for OCs of a similar mass scale. However, such large dispersion values can be partly explained by an observational limitation related to the distance, since both OCs are the most distant of the sample. For a limited observational time-base, the PM determination for a distant OC will primarily detect the high-PM components, thus leading to a broad PM profile and high values of the velocity dispersion. Under similar conditions, a nearby OC, on the other hand, will also have part of the low-PM components detected, thus implying a lower velocity dispersion. This effect is present in our analysis, as can be seen by the correlation between σ_{os} and the distance from the Sun (Fig. 7, left-hand panels). An additional consequence of the distance-related effect would be a shift towards high values of the on-sky average velocity ($\bar{\mu}$). Again, this shift would increase with the distance from the Sun and this relation is also present in Fig. 7. Despite this effect, the average velocity of the bump stars in NGC 2477 ($\bar{\mu} \approx 78\,\mathrm{km\,s^{-1}}$) is exceedingly high for a $\sim 10^3\,M_\odot$ cluster, to the point that these stars – if they really belong to NGC 2477 – are not gravitationally bound to the cluster. This suggests that the high-velocity bump may be an artefact produced by the RL deconvolution (when applied to asymmetric profiles) or, least probably, unaccounted for the field contamination.

Given the above caveat, it is not possible to disentangle a physical relation between σ_{os} and the cluster age (Fig. 7, right-hand panels) from the observational limitation.

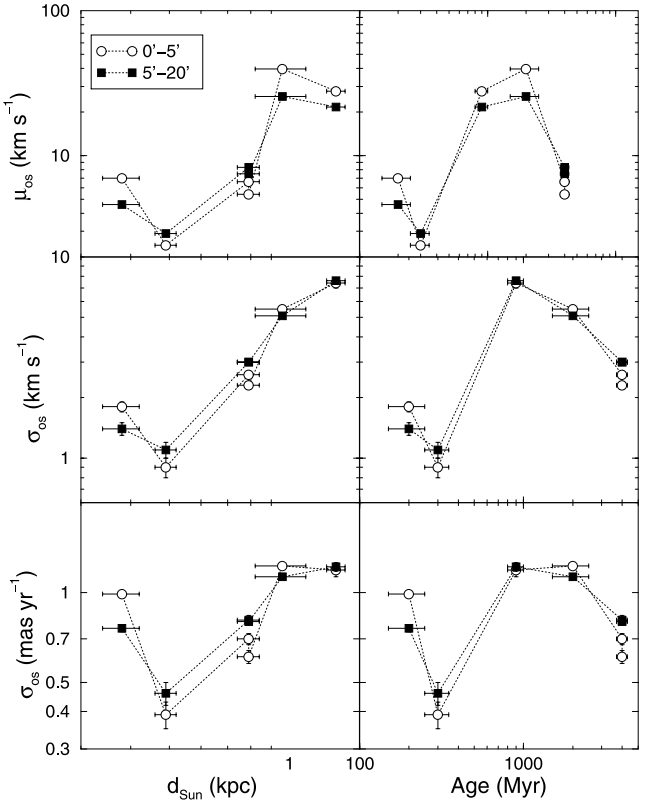

Figure 7. Dependence of the deconvolved profile parameters on the distance from the Sun (left-hand panels) and cluster age (right-hand panels). The central (empty circles) and outer (filled squares) regions are shown. Given the rather limited range of values of $\sigma_{obs}/\sigma_{dec}$ (Table 2), similar relations hold as well for the observed values of $\bar{\mu}$ and σ_{os}.

6 SUMMARY AND CONCLUSIONS

A crucial point in understanding a cluster's dynamical stage is the derivation of kinematical parameters for its member stars, usually by means of PMs obtained in public data bases. However, uncertainties associated with ground-based PM measurements are usually large and their effect should be properly taken into account when building PM profiles for determining the velocity dispersion.

In this paper, we investigate the above issue using the relatively nearby and populous open clusters NGC 1039 (M 34), NGC 2477, NGC 2516, NGC 2682 (M 67) and NGC 7762 as test cases. Their PM components have been obtained in UCAC3.

Rather than working with PM histograms, we build PMDFs for the cluster and field stars, taking the 1σ-PM uncertainties into account. In short, (i) we use the CMD morphology for establishing the colour and magnitude ranges of the probable member stars; (ii) these stars are used to build the RDP, which provides the cluster structural parameters and allows to define the comparison field; (iii) we define a grid of PM bins of variable size that spans the full range of values of $\mu_\alpha \cos(\delta)$, μ_δ and μ_{os}; (iv) considering the cluster and field stars separately, we compute the probability that the PM measurements of a given star correspond to any bin; (v) the field-star PMDF is subtracted from the cluster PMDF; and (vi) we take the intrinsic PM-error distribution function as the PSF to be used in the RL deconvolution approach.

The main result of our approach is that the deconvolved PMDFs are well represented by Gaussians with dispersions lower than the observed ones by a factor of 4–10. Besides the main component,

the deconvolution revealed structure in the profiles of NGC 2477 and 2682 in the form of a second – and less-populous – distribution shifted towards higher average velocities, which may originate from cluster merger, large-scale mass segregation or, least probably, binaries. The secondary bump in NGC 2477 consistently appears in PMDFs built with stars brighter and fainter than $J = 12.5$, which suggests that it is not related to incompleteness and/or faint star PM measurement. However, we cannot exclude the possibility that the bump is an artefact produced by the RL deconvolution when applied to strongly asymmetric profiles such as those of NGC 2477 and 2682. NGC 1039 and 2516, the nearest OCs analysed here, end up with deconvolved dispersions compatible with those expected of bound OCs of $\sim 10^3$ $M_\odot$. We also detect an increase in the velocity dispersion and average velocity with the distance from the Sun, which is probably due to a similarly limited time-base used for measuring the PMs among different star clusters.

In recent years, our group has given particular attention to the investigation of OCs by means of analytical tools that produce field-star decontaminated CMDs and RDPs. These tools have proved essential for a constrained analysis of OCs characterized by a range of parameters (age, distance from the Sun, reddening, etc.), and located on a wide variety of environments (e.g. Bonatto et al. 2006; Bonatto & Bica 2007; Bonatto & Bica 2010b). This paper links the classical CMD and RDP analyses with a novel approach for dealing with PMs and the respective errors.

ACKNOWLEDGMENTS

We thank the referee, Thijs Kouwenhoven, for interesting comments and suggestions. We acknowledge the support from the Brazilian Institution CNPq. This publication makes use of data products from the 2MASS, which is a joint project of the University of Massachusetts and the Infrared Processing and Analysis Centre/California Institute of Technology, funded by the National Aeronautics and Space Administration and the National Science Foundation. We also employed the WEBDA data base, operated at the Institute for Astronomy of the University of Vienna.

REFERENCES

Bi H., Boerner G., 1994, A&AS, 108, 409
Bica E., Bonatto C., 2005, A&A, 431, 943
Bonatto C., Bica E., 2007, MNRAS, 377, 1301
Bonatto C., Bica E., 2009, MNRAS, 394, 2127
Bonatto C., Bica E., 2010a, A&A, 516, 81
Bonatto C., Bica E., 2010b, A&A, 521A, 74
Bonatto C., Bica E., Girardi L., 2004, A&A, 415, 571
Bonatto C., Bica E., Ortolani S., Barbuy B., 2006, A&A, 453, 121
Chen L., de Grijs R., Zhao J. L., 2007, AJ, 134, 1368
de Grijs R., Goodwin S. P., Kouwenhoven M. B. N., Kroupa P., 2008, A&A, 492, 685
de Oliveira M. R., Dutra C. M., Bica E., Dottori H., 2000, A&AS, 146, 57
de Oliveira M. R., Bica E., Dottori H., 2000, MNRAS, 311, 589
Girardi L., Bertelli G., Bressan A., Chiosi C., Groenewegen M. A. T., Marigo P., Salasnich B., Weiss A., 2002, A&A, 391, 195
Goodwin S. P., Bastian N., 2006, MNRAS, 373, 752
Kouwenhoven M. B. N., de Grijs R., 2008, A&A, 480, 103
Lada C. J., Lada E. A., 2003, ARA&A, 41, 57
Lamers H. J. G. L. M., Gieles M., Bastian N., Baumgardt H., Kharchenko N. V., Portegies Zwart S., 2005, A&A, 441, 117
Lucy L., 1974, AJ, 79, 745
Pavani D. B., Bica E., 2007, A&A, 468, 139
Piskunov A. E., Schilbach E., Kharchenko N. V., Röser S., Scholz R.-D., 2007, A&A, 468, 151
Richardson W. H., 1972, J. Opt. Soc. Am., 62, 55
Richer H. B. et al., 2008, AJ, 135, 2141
Skrutskie M. F. et al., 2006, AJ, 131, 1163
Spitzer L., 1987, Dynamical Evolution of Globular Clusters. Princeton Univ. Press, Princeton, NJ, p. 191
Vio R., Bardsley J., Wamsteker W., 2005, A&A, 442, 397
Yadav R. K. S. et al., 2008, A&A, 484, 609
Zacharias N., Monet D. G., Levine S. E., Urban S. E., Gaume R., Wycoff G. L., 2004, A&AS, 205, 4815
Zacharias N. et al., 2010, AJ, 139, 2184

APPENDIX A: SOME ASPECTS RELATED TO THE RICHARDSON–LUCY DECONVOLUTION

A1 PMDF resolution

For preserving the profile resolution especially around the PMDF peak (where the number density of stars is high) and, at the same time, keeping acceptable error bars (especially towards the PMDF wings where the number density is low), we adopt a variable distribution of bin sizes δ_{pm}, where *pm* represents any component among $[\mu_\alpha \cos(\delta)$, μ_δ and $\mu_{os}]$ for building the PMDFs.

After determining where the PMDF peak occurs, we use $\delta_{pm} = 0.25$ mas yr^{-1} for shifts with respect to the peak in the range $|\Delta_{pm}| =$ 0–10 mas yr^{-1}, $\delta_{pm} = 1$ mas yr^{-1} for $|\Delta_{pm}| =$ 10–30 mas yr^{-1}, $\delta_{pm} = 5$ mas yr^{-1} for $|\Delta_{pm}| =$ 30–50 mas yr^{-1}, and $\delta_{pm} =$ 10 mas yr^{-1} for $\Delta_{pm} > 50$ mas yr^{-1} and $\Delta_{pm} < -50$ mas yr^{-1}.

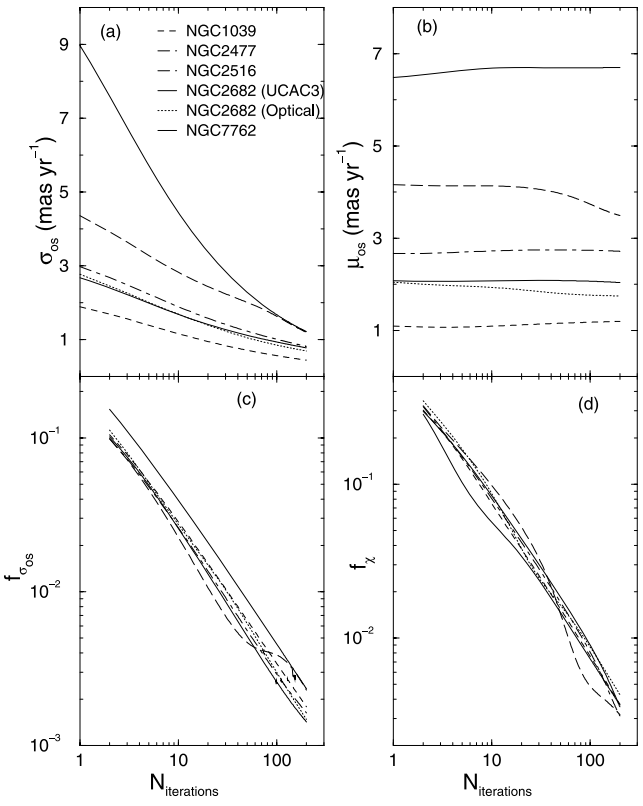

Figure A1. Top panels: variation with the number of deconvolution iterations of the on-sky velocity dispersion σ_{os} (left-hand panel) and average velocity $\bar{\mu}$ (right-hand panel). Bottom panels: fractional variation of σ_{os} (left-hand panel) and χ (right-hand panel). The curves correspond to the 0–20 arcmin PMDFs, except for the optical PMDF of NGC 2682 built for 0–15 arcmin.

Additionally, this procedure also has the advantage of reducing the computation time.

A2 Deconvolution convergence

The rather slow convergence rate of the RL deconvolution method has been extensively discussed in the literature (e.g. Bi & Boerner 1994; Vio, Bardsley & Wamsteker 2005). However, it is easy to implement, reliable, and the quality of the outputs can be followed at each iteration.

We follow in Fig. A1 the changes in σ_{os} and $\bar{\mu}$ with the number of deconvolution iterations (N_{it}). While the average velocity (panel b) changes little over the 200 iterations applied here, σ_{os}, on the other hand, decreases systematically with N_{it} (panel a) but with a rate that begins to flatten for $N_{it} \gtrsim 100$. Clearly, σ_{os} could decrease somewhat more for $N_{it} > 200$. However, as implied by the rate of change $f\sigma_{os} = \Delta\sigma_{os}/\sigma_{os}$ that, for $N_{it} = 200$, has decreased to $f\sigma_{os} \lesssim 0.003$ (panel c), it would take several hundred more iterations to produce a significant change in σ_{os}. Finally, the χ^2 (Section 4) fractional variation $f_\chi = \Delta\chi/\chi$ also presents a steady decrease with N_{it} (panel d), dropping to $f_\chi \sim 0.003$ (or a ∼0.3 per cent variation) for $N_{it} = 200$.

APPENDIX B: OBSERVED AND FIELD PROPER MOTION DISTRIBUTION FUNCTIONS

We show in Figs B1 and B2 the observed on-sky PMDFs for all clusters of our sample, built for the central, outer and overall cluster

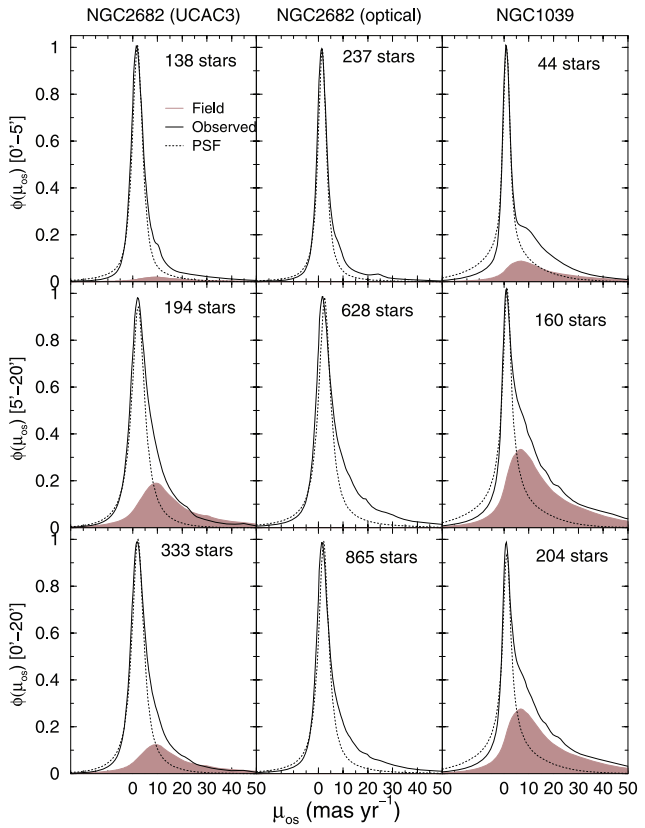

Figure B1. The panels show the observed, field, and intrinsic error (PSF) on-sky PMDFs built for different cluster regions: central (top panels), outer (middle panels) and overall (bottom panels). The number of member stars in each region is indicated.

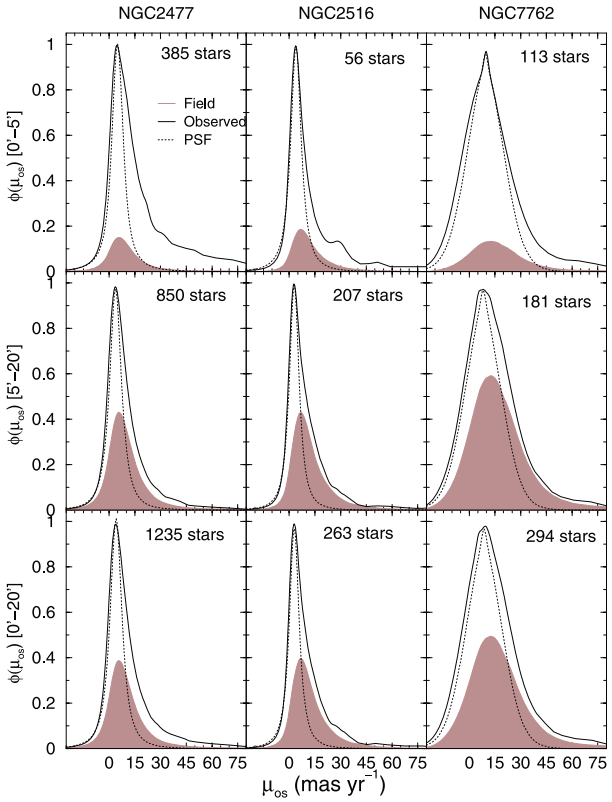

Figure B2. Same as Fig. B1 for the remaining OCs.

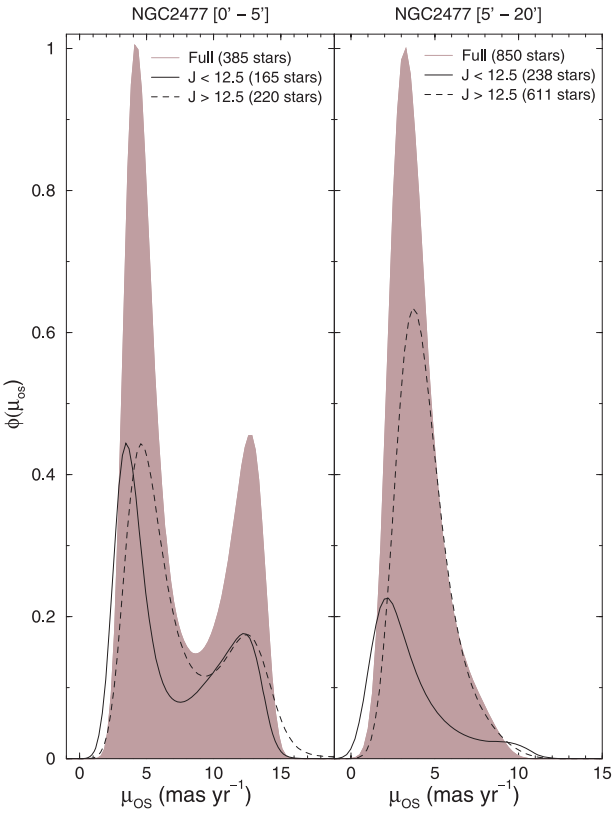

Figure B3. Deconvolved PMDFs for the central and outer regions of NGC 2477, separated by magnitude ranges. The bright (solid line) and faint (dashed) PMDFs are compared to the 'full-magnitude' (shaded) PMDF. The number of stars composing the PMDFs is indicated.

regions. Also shown are the PMDFs corresponding to the intrinsic error distribution (PSF) and the field. It is interesting to note the relative contribution of the field-star PM among the different regions of the same cluster and among the full set of clusters. This shows that the field contribution must be taken into account in the analysis. Also, and perhaps more importantly, is the PSF width that, in some cases, is almost as broad as the cluster PMDF.

B1 PMDFs in different magnitude ranges

In Fig. B3, we examine the incompleteness/faint stars' issue in NGC 2477, which should be important especially for the central part of the cluster. Starting with the CMD of NGC 2477 (Fig. 2), we build PMDFs separately for stars brighter and fainter than $J = 12.5$. This magnitude boundary is adequate for characterizing different types of stars and, at the same time, keeping a reasonable number of stars in each magnitude range. The bright and faint PMDFs are compared to the 'full-magnitude' range PMDF, both for the central (left-hand panels) and outer (right-hand panels) cluster regions.

This paper has been typeset from a TEX/LATEX file prepared by the author.